Piecewise Convex Multiple-Model Endmember Detection and Spectral Unmixing

Alina Zare, *Member, IEEE*, Paul Gader, *Fellow, IEEE*, Ouiem Bchir, and Hichem Frigui, *Member, IEEE*

Abstract—A hyperspectral endmember detection and spectral unmixing algorithm that finds multiple sets of endmembers is presented. Hyperspectral data are often nonconvex. The Piecewise Convex Multiple-Model Endmember Detection algorithm accounts for this using a piecewise convex model. Multiple sets of endmembers and abundances are found using an iterative fuzzy clustering and spectral unmixing method. The results indicate that the piecewise convex representation estimates endmembers that better represent hyperspectral imagery composed of multiple regions where each region is represented with a distinct set of endmembers.

Index Terms—Clustering functional forms, endmember, fuzzy, hyperspectral, image analysis, non-linear unmixing, piece-wise convex, scene analysis, scene segmentation, unmixing.

I. INTRODUCTION

THE standard model used to perform hyperspectral unmixing and endmember extraction is the *linear mixing model* as shown in

$$\mathbf{x}_i = \sum_{k=1}^{M} p_{ik} \mathbf{e}_k + \epsilon_i, \qquad i = 1, \ldots, N \qquad (1)$$

where N is the number of pixels in the image, M is the number of endmembers, ϵ_i is an error term, p_{ik} is the proportion of endmember k in pixel i, and $\mathbf{e}_k$ is the kth endmember [1]. The proportions of this model satisfy the constraints in

$$p_{ik} \geq 0 \qquad \forall k = 1, \ldots, M$$
$$\sum_{k=1}^{M} p_{ik} = 1. \qquad (2)$$

Generally, when applying the linear mixing model with a single set of endmembers, input pixels are assumed to be linear mixtures of all endmembers in the scene. Many endmember

A. Zare is with the Department of Electrical and Computer Engineering, University of Missouri, Columbia, MO 65211 USA (e-mail: zarea@missouri.edu).
P. Gader is with the Department of Computer and Information Science and Engineering, University of Florida, Gainesville, FL 32611 USA (e-mail: pgader@cise.ufl.edu).
O. Bchir is with the Computer Science Department, College of Computer and Information Sciences, King Saud University, Riyadh 11543, Saudi Arabia (e-mail: o0bchi01@louisville.com).
H. Frigui is with the Department of Computer Engineering and Computer Science, University of Louisville, Louisville, KY 40292 USA (e-mail: h.frigui@louisville.edu).

detection and spectral unmixing algorithms which rely on the linear mixing model have been proposed in the literature [1]–[3]. A number of these methods make the pixel purity assumption and assume that the endmembers can be found within the data set [4]–[10]. Methods have also been developed based on nonnegative matrix factorization [11]–[14], independent component analysis [15], [16], and others [17]–[21]. In the results shown here, comparisons are made to the vertex component analysis (VCA) and iterative constrained endmembers (ICE) algorithms [6], [19]. The VCA algorithm is an iterative algorithm that relies on the pixel purity assumption and selects endmembers from the input scene. The ICE algorithm estimates "virtual" endmembers and is, therefore, capable of estimating endmembers for highly mixed scenes. However, all of these methods (including VCA and ICE) search for a single set of endmembers and, therefore, a single convex region to describe a hyperspectral scene. Since these algorithms assume a single convex region, they often cannot find appropriate endmembers for nonconvex data sets.

Piecewise Convex Multiple-Model Endmember Detection (PCOMMEND) extends the linear mixing model to multiple sets of endmembers. Consider a scene that contains multiple distinct regions that do not share common materials. Each region in this scene is composed of pixels that are linear mixtures of a distinct set of endmembers, and each of these endmember sets defines a simplex. Then, the set of all image spectra will consist of a union of all of the simplices. The union of simplices is unlikely to be convex. For scenes of this type, a piecewise convex model with multiple sets of endmembers is more appropriate than the linear mixing model with a single convex region.

Spectral unmixing methods that account for spectral variability or use per-pixel specific endmember sets to unmix hyperspectral data have been previously developed in the literature [2]. These methods include a Monte Carlo unmixing approach that determines the mean and variance of abundance values computed using randomly selected endmembers [22]. Also, "endmember bundles" have been investigated to address endmember variability. An endmember bundle is a set of spectra from one material. These bundles are often formed from field measurements, pulled from spectral libraries, or pulled from an imaged scene [23], [24]. The multiple-endmember spectral mixture analysis algorithm has been used extensively to account for endmember variability and allow for per-pixel specific endmembers [25]. Methods based on the normal compositional model, which account for spectral variability of the endmembers by representing endmembers using Gaussian distributions, have also been developed in [26]–[29].

Incorporating spectral variability and per-pixel specific end-member sets differs from the PCOMMEND in that the proposed method estimates distinct endmember sets for groups of pixels (rather than on a per-pixel level). PCOMMEND focuses on identifying regions in the scene that are composed of the same set of endmembers. Currently, PCOMMEND uses a single spectrum for each endmember. However, future work to incorporate spectral variability into PCOMMEND and merge these approaches will be conducted.

Endmember extraction methods that represent hyperspectral imagery using a piecewise convex representation or using multiple clusters of data have been previously published. A piecewise convex representation for hyperspectral imagery was previously developed in [27], [28], and [30]. These methods sample from a Dirichlet process to partition the input hyperspectral data into convex regions.

Section II develops and describes PCOMMEND. Section III includes experimental results on simulated and real hyperspectral data sets. Finally, Section IV includes discussion and future work.

II. PCOMMEND

PCOMMEND estimates endmember sets and proportion values by minimizing the objective function shown in

$$
J(\mathbf{E}, \mathbf{P}, \mathbf{U}) = \sum_{i=1}^{C} \left(\sum_{j=1}^{N} u_{ij}^m (\mathbf{x}_j - \mathbf{E}_i \mathbf{p}_{ij})^{\mathrm{T}} (\mathbf{x}_j - \mathbf{E}_i \mathbf{p}_{ij}) \right.
$$
$$
\left. + \alpha \sum_{k=1}^{M-1} \sum_{j=k+1}^{M} (\mathbf{e}_{ik} - \mathbf{e}_{ij})^{\mathrm{T}} (\mathbf{e}_{ik} - \mathbf{e}_{ij}) \right)
\tag{3}
$$

such that

$$
p_{ijk} \geq 0 \qquad \forall k = 1, \ldots, M
$$
$$
\sum_{k=1}^{M} p_{ijk} = 1
\tag{4}
$$
$$
u_{ij} \geq 0 \qquad \forall k = 1, \ldots, M
$$
$$
\sum_{i=1}^{C} u_{ij} = 1
\tag{5}
$$

where $\mathbf{x}_j$ is a $d \times 1$ column vector representing the jth pixel, C is the number of endmember sets being estimated, $\mathbf{p}_{ij}$ is the vector of proportion values associated with pixel j for the ith endmember set, $\mathbf{E}_i$ is a $d \times M$ matrix such that each column of $\mathbf{E}_i$, i.e., $\mathbf{e}_{ik}$, is the $d \times 1$ vector representing the kth endmember in the ith endmember set, weight u_{ij} is the membership value of the jth data point in the ith endmember set, α is a fixed parameter used to balance the two terms of the objective function, and m is a fixed parameter which controls the degree of sharing across endmember sets.

The first term of this objective function computes the squared Euclidean distance between each input hyperspectral data point and their estimate using the estimated endmembers and proportion values. The second term is used to constrain the size of each simplex by minimizing the squared Euclidean distance between each pair of endmembers in an endmember set. The membership values u_{ij} in the first term indicate the degree

to which pixel j is represented by the endmembers of convex set i. Note that, if $C = 1$, this is essentially the ICE algorithm objective function [19].

Endmembers, proportions, and membership values are estimated using alternating optimization. All values are initialized, and then, the endmembers, proportions, and membership values are updated iteratively. Solving $\partial J / \partial \mathbf{E}_i = 0$ results in the following update equation for the endmembers:

$$
\mathbf{E}_i = \left(\sum_j u_{ij}^m \mathbf{p}_{ij} \mathbf{p}_{ij}^{\mathrm{T}} + 2\alpha (M\mathbf{I}_{M \times M} - \mathbf{1}_{M \times M}) \right)^{-1}
$$
$$
\times \left(\sum_j u_{ij}^m \mathbf{p}_{ij} \mathbf{x}_j^{\mathrm{T}} \right)
\tag{6}
$$

where $\mathbf{I}_{M \times M}$ is an $M \times M$ identity matrix and $\mathbf{1}_{M \times M}$ is an $M \times M$ matrix of ones. Minimizing the objective function J with respect to $\mathbf{p}_{ij}$ by adding a Lagrange multiplier term to enforce the sum-to-one constraint and applying the Karush–Kuhn–Tucker conditions [31] to enforce the nonnegativity constraints on the proportion values results in the following update for the proportion values:

$$
\mathbf{p}_{ij} = \max \left(\left(\mathbf{E}_i^{\mathrm{T}} \mathbf{E}_i \right)^{-1} \left(\mathbf{E}_i^{\mathrm{T}} \mathbf{x}_j - \frac{\lambda_i}{2} \mathbf{1}_{M \times 1} \right), 0 \right)
\tag{7}
$$

where

$$
\lambda_i = 2 \frac{\mathbf{1}_{1 \times M} \left(\mathbf{E}_i^{\mathrm{T}} \mathbf{E}_i \right)^{-1} \mathbf{E}_i^{\mathrm{T}} \mathbf{x}_j - 1}{\mathbf{1}_{1 \times M} \left(\mathbf{E}_i^{\mathrm{T}} \mathbf{E}_i \right)^{-1} \mathbf{1}_{M \times 1}}.
\tag{8}
$$

If the proportion values are clipped at zero, then the values are renormalized following this step to ensure that they sum to one.

Finally, the update equation for the membership values is found by adding a Lagrange multiplier term to enforce the sum-to-one constraint on the membership values

$$
u_{ij} = \frac{\left(\frac{1}{(m-1)(\mathbf{x}_j - \mathbf{E}_i \mathbf{p}_{ij})^{\mathrm{T}} (\mathbf{x}_j - \mathbf{E}_i \mathbf{P}_{ij})} \right)^{\frac{1}{m-1}}}{\sum_{q=1}^{C} \left(\frac{1}{(\mathbf{x}_j - \mathbf{E}_q \mathbf{p}_{qj})^{\mathrm{T}} (\mathbf{x}_j - \mathbf{E}_q) \mathbf{p}_{qj}} \right)^{\frac{1}{m-1}}}.
\tag{9}
$$

The proposed PCOMMEND algorithm is summarized in the following.

Algorithm 1 PCOMMEND

Set the number of endmember sets C, the number of endmembers per set M, and the parameters m and α
    Initialize the membership values $\mathbf{U}$
    Initialize the proportions $\{\mathbf{p}_{ij}\}_{i=1,\ldots,C; j=1,\ldots,N}$
      REPEAT
          Update endmember matrices $\{\mathbf{E}_i\}_{i=1,\ldots,C}$ using (6)
          Update the set of abundances $\{\mathbf{p}_{ij}\}_{i=1,\ldots,C; j=1,\ldots,N}$ using (7) and (8) and renormalize
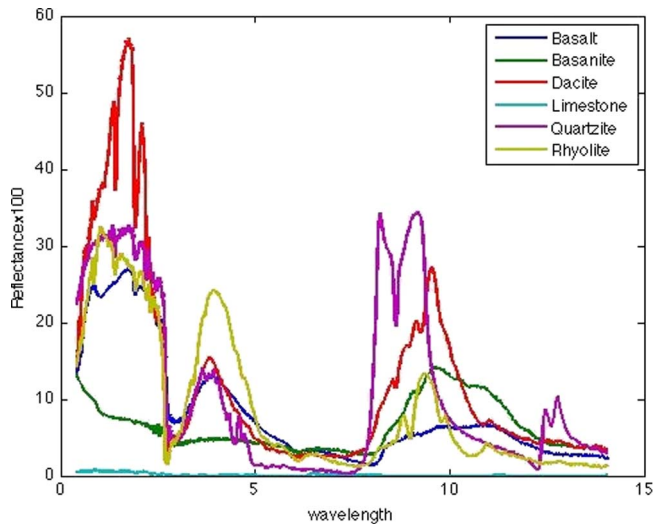   Update the memberships using (9)
      UNTIL convergence

Fig. 1. Spectral signatures for Limestone (CaCO₃), Basalt, Quartzite, Basanite, Rhyolite, and Dacite from the ASTER spectral library. These library spectra were used to generate simulated hyperspectral data. The wavelength values are in nanometers.

In the current implementation of the algorithm, the endmembers are initialized by randomly selecting input hyperspectral pixels. The proportion values are randomly initialized by drawing from a uniform Dirichlet distribution. The membership values are initialized using the fuzzy c-means algorithm (which is, in turn, randomly initialized). Furthermore, convergence is checked by comparing the differences between the $\mathbf{E}$, $\mathbf{P}$, and $\mathbf{U}$ from successive iterations. If the total difference is below some threshold, the algorithm is stopped. Also, in the current implementation, the C and M parameters are set manually. Investigations on how to set these parameters using cluster validity approaches have been conducted in [32]. Further work on autonomously setting these parameters will be conducted.

III. EXPERIMENTAL RESULTS

In the following, PCOMMEND is tested using simulated and measured hyperspectral data sets. The first data set is a simulated data set generated from the Advanced Spaceborne Thermal Emission and Reflection Radiometer (ASTER) spectral library. This data set is used to compare PCOMMEND to the ICE and VCA algorithms given that the true endmembers and proportion values are known. Following the simulated data sets, two real data sets are used to evaluate the algorithm: HySens Pavia University data and Landsat Thematic Mapper (TM) data.

A. Simulated Hyperspectral Data

PCOMMEND was applied to simulated hyperspectral data generated using the ASTER spectral library [33]. Spectra for the minerals Limestone (CaCO₃), Basalt, Quartzite, Basanite, Rhyolite, and Dacite were used to generate 1000 spectra. The experiments conducted with simulated data were conducted to test the sensitivity to noise and the initialization of PCOMMEND and provide comparison to the VCA and ICE algorithms. The spectra are shown in Fig. 1. Each simulated hyperspectral pixel was a convex combination of endmembers

A, B, and C or a convex combination of X, Y, and Z. The proportions for each data point were generated by sampling from a Dirichlet distribution with a mean value of [1/3, 1/3, 1/3] and a variance of [0.02, 0.02, 0.02], resulting in proportion values that ranged from 0.02 to 0.85. Therefore, this data set was highly mixed and did not include any pure spectra. Zero-mean Gaussian noise was added to the simulated spectra at three noise levels. The noise levels were adjusted by changing the variance of the Gaussian noise, resulting in average SNR values of 62, 48, and 42 dB for the three levels.

PCOMMEND was run 25 times with random initialization and the addition of Gaussian random noise at the three levels as discussed earlier. Table I shows the mean and standard deviation of the endmember estimation error across the 25 runs using the spectral angle distance (SAD) [34]. The SAD error shown in the table was computed by first pairing the estimated endmembers to true endmembers used to generate the data. After finding the best match between the endmember sets, SAD was computed between each pair and summed across all pairs to produce the value shown in the table. A similar process was used for the remaining results computed using spectral information divergence (SID) [35] and the squared error between endmembers and proportions. The mean SID value was computed by summing the SID values over endmembers and averaging across 25 runs of the algorithm. Table II shows the results using SID. Table III shows the results for the squared error between the estimated and true endmember values. The mean squared error between the endmembers was computed by summing the squared errors between the true and estimated endmembers over the wavelength and then averaging across the 25 runs. Table IV shows the results for the squared error between the estimated and true proportion values. The mean squared error between the endmembers was computed by summing the squared errors between the true and estimated proportions over all data points and proportion values and then averaging across the 25 runs. The error on the proportion values was only computed using PCOMMEND and ICE since VCA does not estimate proportion values.

Examining these results, we see that PCOMMEND consistently outperforms the other algorithms on this piecewise convex and highly mixed data set. The authors have found VCA to be fast and accurate for data sets that contain pure pixels including piecewise convex hyperspectral data sets in which no endmember can be described using convex combinations of the other endmembers. However, since these data were generated with proportion values that do not exceed 0.85, methods that are appropriate for highly mixed data sets (such as PCOMMEND and ICE) can outperform VCA. PCOMMEND also outperforms ICE on average over the 25 runs for each noise level due to the piecewise convexity of the data. Both PCOMMEND and ICE are initialization dependent. However, since PCOMMEND is able to represent the piecewise convexity of the data, it can consistently estimate appropriate endmembers for the set.

The average running time was recorded for each algorithm on versions of these data with increasing levels of noise. Table V shows the average running time until convergence for increasing levels of noise on a machine with a 2.26-GHz processor and a 12-GB RAM. All algorithms were coded in MATLAB, but the

TABLE I
ASTER SIMULATED HYPERSPECTRAL DATA RESULTS WITH INCREASING NOISE AND RANDOM INITIALIZATION MEAN SAD
(± 1 STANDARD DEVIATION OVER 25 RUNS) BETWEEN THE ESTIMATED AND TRUE ENDMEMBERS

Average SNR	PCOMMEND Results	VCA Results	ICE Results
62 db SNR	**0.25 ± 0.18**	0.35 ± 0.31	0.89 ± 0.33
48 db SNR	**0.25 ± 0.17**	0.34 ± 0.18	0.81 ± 0.40
42 db SNR	**0.32 ± 0.15**	0.32 ± 0.14	1.04 ± 0.49

TABLE II
ASTER SIMULATED HYPERSPECTRAL DATA RESULTS WITH INCREASING NOISE AND RANDOM INITIALIZATION MEAN SID
(± 1 STANDARD DEVIATION OVER 25 RUNS) BETWEEN THE ESTIMATED AND TRUE ENDMEMBERS

Average SNR	PCOMMEND Results	VCA Results	ICE Results
62 db SNR	**32.7 ± 18.1**	170.9 ± 42.9	186.3 ± 181.3
48 db SNR	**33.6 ± 17.5**	169.2 ± 61.0	154.7 ± 113.1
42 db SNR	**40.9 ± 16.0**	121.9 ± 40.9	227.4 ± 139.8

TABLE III
ASTER SIMULATED HYPERSPECTRAL DATA RESULTS WITH INCREASING NOISE AND RANDOM INITIALIZATION MEAN SQUARED
ERROR (± 1 STANDARD DEVIATION OVER 25 RUNS) BETWEEN THE ESTIMATED AND TRUE ENDMEMBERS

Average SNR	PCOMMEND Results	VCA Results	ICE Results
62 db SNR	**6.2 ± 3.1**	25.0 ± 3.1	19.2 ± 9.1
48 db SNR	**6.0 ± 2.6**	24.7 ± 3.9	20.5 ± 14.8
42 db SNR	**6.9 ± 2.1**	21.5 ± 4.0	26.7 ± 17.3

TABLE IV
ASTER SIMULATED HYPERSPECTRAL DATA RESULTS WITH INCREASING
NOISE AND RANDOM INITIALIZATION MEAN SQUARED ERROR
(± 1 STANDARD DEVIATION OVER 25 RUNS) BETWEEN THE
ESTIMATED AND TRUE PROPORTION VALUES

Average SNR	PCOMMEND Results	ICE Results
62 db SNR	**21.3 ± 7.3**	54.7 ± 25.1
48 db SNR	**21.5 ± 6.9**	56.1 ± 27.9
42 db SNR	**24.7 ± 6.6**	70.4 ± 31.2

quadratic program portion of ICE was coded in C. The average running times are relative given that the experiments were not conducted on a dedicated machine.

B. HySens Pavia University Data

In addition to the simulated data discussed earlier, two measured data sets were unmixed using PCOMMEND. The first was a Reflective Optics System Imaging Spectrometer (ROSIS) Pavia University data set collected on July 8, 2002. These hyperspectral data were collected over an urban area of Pavia, in northern Italy, by the ROSIS. The image contains 610 × 340 pixels with 103 bands. The ROSIS sensor collected the data over the 430–850-nm wavelength range at a 4-nm spectral sampling interval. The instantaneous field of view of the sensor is 0.56 mrad with a total field of view of $\pm 8°$. The data shown are in reflectance and were atmospherically corrected by the German Remote Sensing Data Center of the German Aerospace Center (DLR). Holzwarth *et al.* provide more information on the sensor and preprocessing steps [36]. The image contains both natural and urban regions as shown in Fig. 2.

PCOMMEND was applied to these data with the parameter settings of $\alpha = 0.001$, $M = 3$, $C = 2$, and $m = 2$, resulting in two sets of three endmembers.

For comparison, the ICE and VCA algorithms were applied to this data set as well. The parameter setting used in the ICE algorithm was $\mu = 0.001$. All algorithms were set to estimate six endmembers. All three methods were run ten times with random initialization. The best results (identified by having well-separated distinct endmembers) from each method are shown here.

The endmembers found by PCOMMEND for these data are shown in Fig. 3(a), and the associated proportion maps are shown in Fig. 4. Fig. 5 shows the scatter plots of the first two principal components of the data and the endmembers estimated. The endmembers estimated by VCA and ICE are shown in Fig. 3(b) and (c), respectively. The proportion maps estimated by the ICE algorithm are shown in Fig. 6. The endmembers found by VCA were used to unmix the data with the quadratic program method used in ICE. The proportion maps associated with the endmembers found by VCA are shown in Fig. 7. Also, the scatter plots of the first two principal components of the data and the endmembers estimated by ICE and VCA are shown in Fig. 8.

By examining the results from all the three methods, we can qualitatively evaluate how effective each method was at identifying various materials in the scene. First, considering the scatter plots shown in Fig. 5, we can see that PCOMMEND was effective at splitting the data into two convex regions where convex region 1 was defined by endmembers 1, 2, and 5 and convex region 2 was defined by endmembers 3, 4, and 6. Considering the proportion maps associated with each of the convex regions, we see that PCOMMEND split the data into man-made materials in convex region 1 and natural materials in convex region 2. In the following, we consider six material types identified in the Pavia University image and the methods' relative performance in unmixing with respect to these materials.

1) Metal Roofing: All three methods are able to identify and extract an endmember associated with metal roofing. By comparing the endmember plots in Fig. 3, the first endmembers across all three methods have very similar spectral shapes with a peak around 510 nm. When comparing the proportion maps for the first endmembers in all three methods, we claim that the VCA algorithm was the most effective at identifying the metal roof endmember. This was determined by noticing that the associated VCA proportion map has a large constant value over the metal roof for endmember 1. In contrast, both PCOMMEND and ICE have gaps in the proportion maps for

TABLE V
AVERAGE RUNNING TIME (IN SECONDS; ± 1 STANDARD DEVIATION OVER 25 RUNS) ON THE ASTER SIMULATED
HYPERSPECTRAL DATA RESULTS WITH INCREASING NOISE AND RANDOM INITIALIZATION

Average SNR	PCOMMEND	VCA	ICE
62 db SNR	65.2 ± 15.2	24.2 ± 5.1	$\mathbf{6.5 \pm 1.9}$
48 db SNR	65.7 ± 14.9	17.7 ± 2.2	$\mathbf{6.1 \pm 0.9}$
42 db SNR	55.6 ± 15.3	16.6 ± 2.0	$\mathbf{6.9 \pm 1.2}$
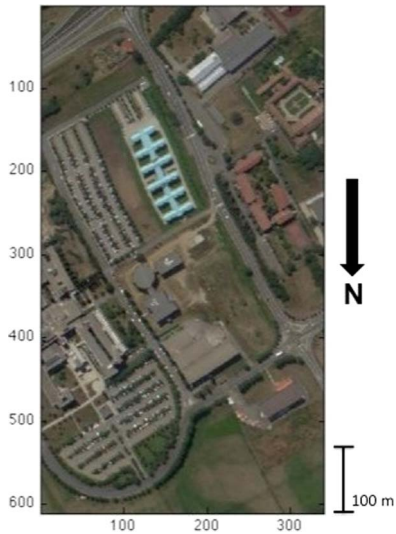
Fig. 2. Image of the ROSIS Pavia University data set (using wavelengths of 661.9, 548, and 476 nm for the red, green, and blue channels to create the color image) collected over Pavia, Italy.

the metal roof. The metal roof in the image has several pure pixels in the scene which VCA identifies. VCA is very effective at finding the endmembers for pure materials, whereas both PCOMMEND and ICE assume highly mixed data sets.

2) Cement/Sidewalk: The second endmember extracted by PCOMMEND, the fourth endmember extracted by VCA, and the fifth endmember extracted by ICE correspond to the cement and sidewalk materials in the Pavia University image. ICE and PCOMMEND find similar spectral shapes for the cement/sidewalk endmember. All three methods had some response over asphalt regions in the cement/sidewalk proportion maps. One item of note is that VCA has less dynamic range in the proportion map associated with cement when compared to the ICE or PCOMMEND results (i.e., higher proportion values throughout the image including pixels that do not contain cement/sidewalk). However, VCA was more effective at unmixing the sidewalk surrounding the metal-roof building, whereas ICE and PCOMMEND have gaps in the proportion maps for this sidewalk-filled area.

3) Shadow: The third endmembers in all three methods were associated with shadows in the imagery. All three methods have some nonzero proportion values associated with shadow over asphalt regions in the proportion maps. However, the VCA proportion map for shadow provides the least error over nonshadow regions such as bare soil. ICE performed the worst at distinguishing shadow from other dark materials in the scene. The ICE shadow proportion map includes strong values over asphalt and bare soil.

4) Bare Soil: The fourth endmembers identified by PCOMMEND and ICE are associated with bare soil in the
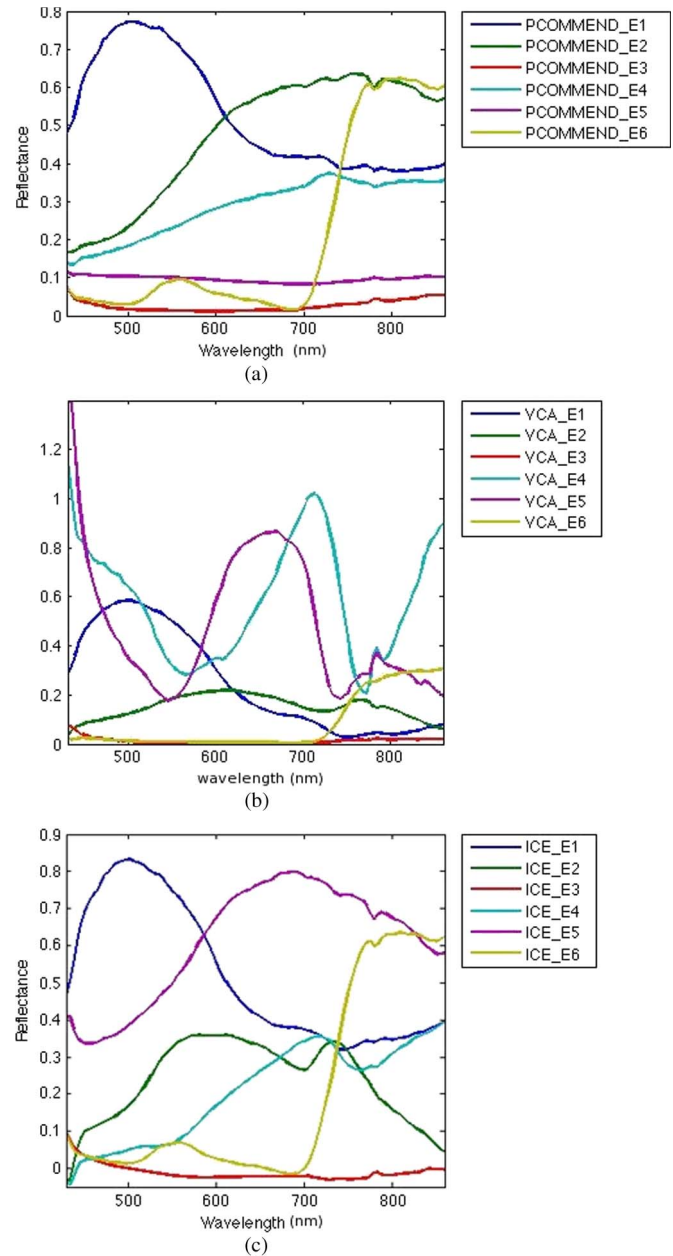

Fig. 3. Endmembers estimated by the (a) PCOMMEND, (b) VCA, and (c) ICE algorithms from the HySens Pavia University image.

scene. Both PCOMMEND and ICE find very similar bare soil endmembers as can be seen in Fig. 3(a) and (c) and the scatter plots in Figs. 5 and 8. When considering the scatter plots, we see that the bare soil endmember is an "interior" endmember. Interior endmembers cannot be extracted by VCA which assumes that endmembers can only be identified as extrema of the entire data set. The fact that VCA does not identify a bare soil endmember can also be explained by the fact that the soil
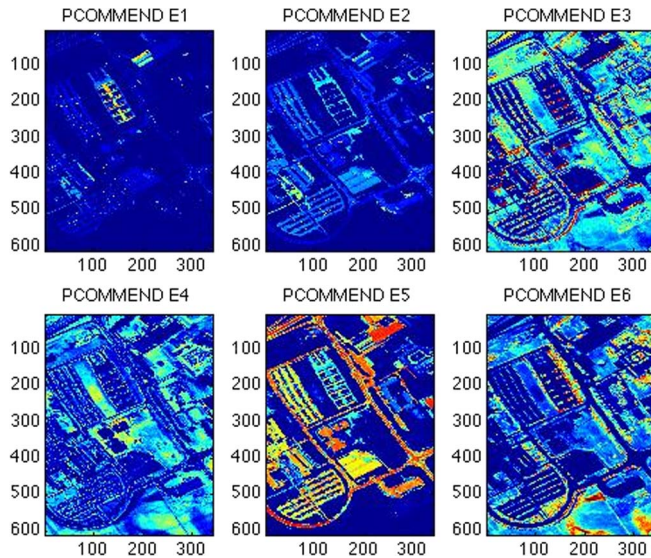
Fig. 4. Proportion maps estimated by the PCOMMEND algorithm from the HySens Pavia University image. Each pixel in the proportion maps was multiplied by the corresponding membership value for each convex region such that the endmembers with high membership for each data point are highlighted. The proportion maps associated with endmembers 1, 2, and 5 correspond to partition 1, and those associated with endmembers 3, 4, and 6 correspond to partition 2. Note that partition 1 can be interpreted as endmembers corresponding to man-made materials and partition 2 can be interpreted as endmembers corresponding to natural materials. The color scale ranges from (dark blue) zero to (red) one.
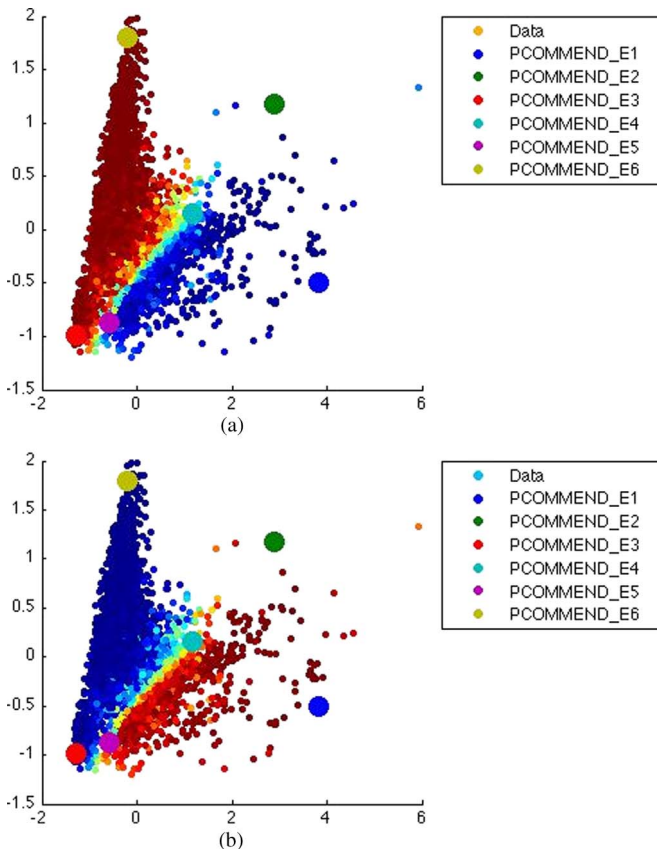

Fig. 5. Proportion maps estimated by the VCA algorithm from the HySens Pavia University image. The color scale ranges from (dark blue) zero to (red) one.
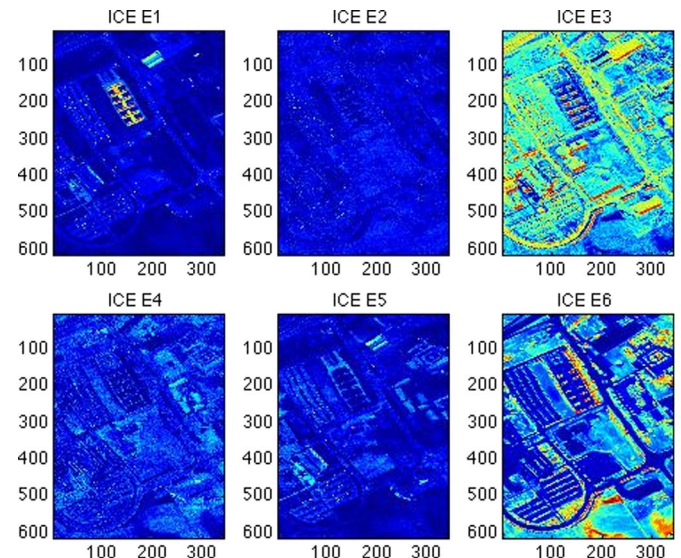

Fig. 6. Proportion maps estimated by the ICE algorithm from the HySens Pavia University image. The color scale ranges from (dark blue) zero to (red) one.
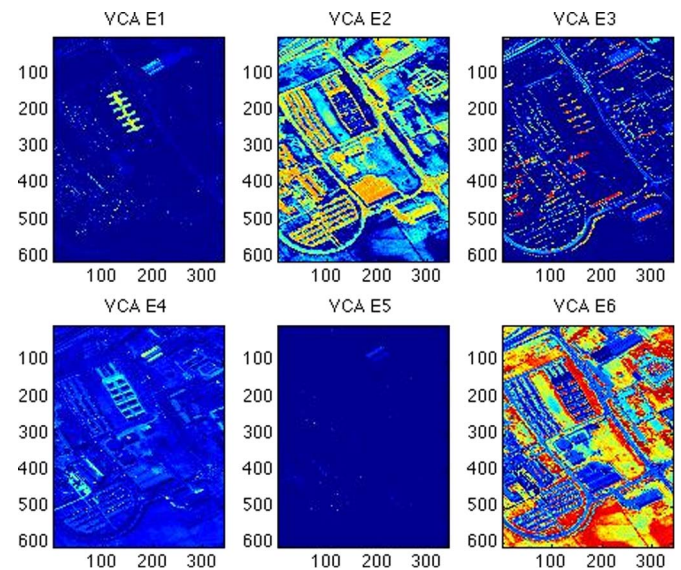

Fig. 7. Scatter plots of the first two principal components of the HySens Pavia University image and the endmembers estimated by the (a) ICE and (b) VCA algorithms. Endmembers shown as large colored circles corresponding to the legend included in the plots.

pixels in the scene are highly mixed with grasses and trees, and VCA is only effective at identifying pure materials. The bare soil pixels in the scene are grouped by VCA with the grass and tree pixels.

Although both PCOMMEND and ICE identify a bare soil endmember, PCOMMEND estimates a more accurate proportion map for the material. By comparing their proportion maps for bare soil, we see that ICE has low proportion values across the bare soil pixels, many gaps, and "noise" in the corresponding proportion map. In contrast, the PCOMMEND proportion map has large proportion values over the bare soil pixels. This difference can be accounted for by considering the objective functions used in the two methods. The PCOMMEND objective
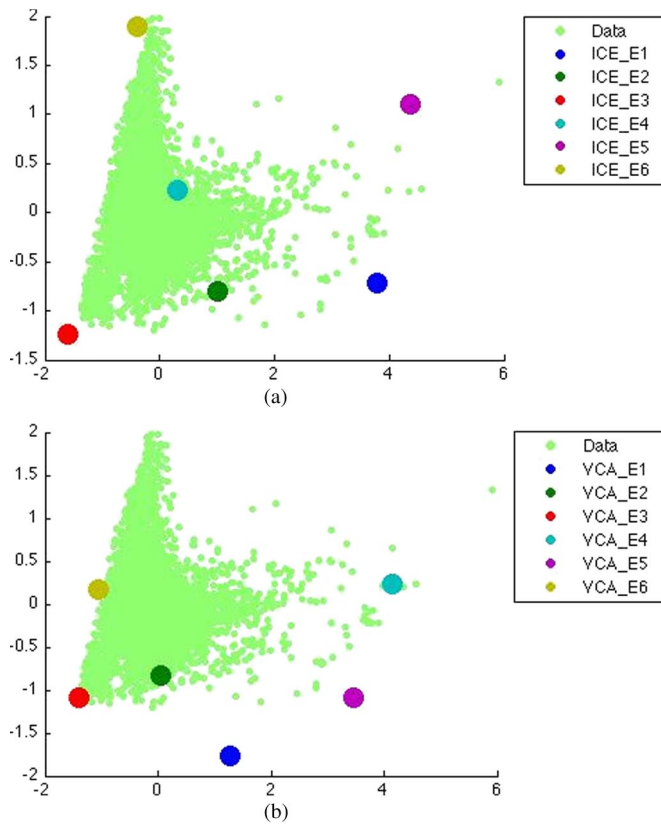
(a)

(b)

Fig. 8. Scatter plots of the first two principal components of the HySens Pavia University image and the endmembers estimated by the PCOMMEND algorithm. The endmembers are shown as large colored circles and correspond to the legend in the upper right of each plot. Color scale corresponding to the membership value (u_{ij}) estimated for each pixel for the set of endmembers shown in each plot (red corresponds to large membership values, and blue corresponds to small membership values). A membership value of zero indicates that the pixel is not composed of the endmembers for the corresponding convex region. Subplot (a) shows the plot with the membership values corresponding to the first convex region (endmembers 3, 4, and 6), and subplot (b) shows the plot with the membership values corresponding to the second convex region (endmembers 1, 2, and 5).
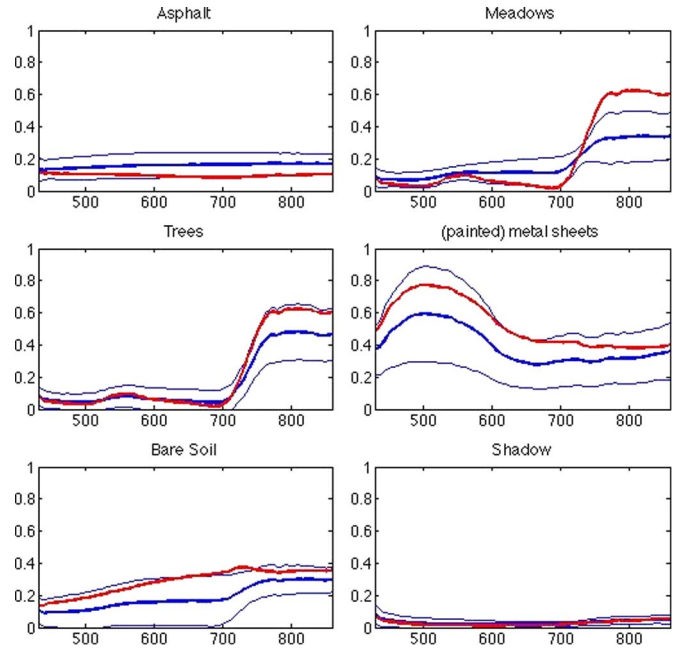

Fig. 9. Comparison between the PCOMMEND endmembers found and the hand-labeled Pavia University ground-truth pixels. The PCOMMEND endmembers are shown in red. The mean spectrum and ± 1 standard deviation of the pixels from the ground-truth class in the Pavia University test set are shown in blue. The x-axis corresponds to the wavelength (in nanometers), and the y-axis is in reflectance.

Fig. 10. Red–green–blue image of the Landsat TM data collected over the coast of Florida. This image was created with the red channel corresponding to $\sqrt{(1/4)(B_3 + B_5 + B_6)}$, the green channel corresponding to $\sqrt{B_1}$, and the blue channel corresponding to $\sqrt{(3/4)B_2 + (1/4)B_4}$, where B_i is the ith band of the Landsat TM image.

function incorporates the piecewise convex representation of the image and only unmixes pixels with a subset of the endmembers in the scene. In contrast, ICE uses all endmembers to unmix the scene, and as a result, the proportions associated with bare soil pixels are spread across multiple endmembers.

5) Asphalt: The fifth endmember identified by PCOMMEND is associated with asphalt. The PCOMMEND proportion map for this endmember highlights the roads and parking lots in the scene. The second endmember estimated by VCA is associated with asphalt. However, when comparing the PCOMMEND and VCA proportion maps for their respective asphalt endmembers, it can be seen that PCOMMEND does not confuse asphalt with bare soil in the scene whereas VCA does. This can be attributed to the fact that PCOMMEND incorporates the piecewise convex representation and, as a result, separates man-made materials from natural materials. ICE was not effective at identifying an asphalt endmember and groups asphalt with shadow and bare soil in the scene.

6) Vegetation: The sixth endmember estimated by PCOMMEND was the vegetation endmember associated with grass and trees in the scene. In Fig. 3(a), we see that the sixth

endmember has a strong red-edge feature which is expected for vegetation. The sixth endmembers found by ICE and VCA are also associated with vegetation. However, the VCA algorithm is less effective at separating vegetation from bare soil than the other two methods since VCA was unable to estimate an endmember associated with bare soil.

ICE and VCA identify additional endmembers (ICE_E2 and VCA_E5) in addition to these materials. However, neither of these endmembers has large proportion values for significant and identifiable areas in the scene.
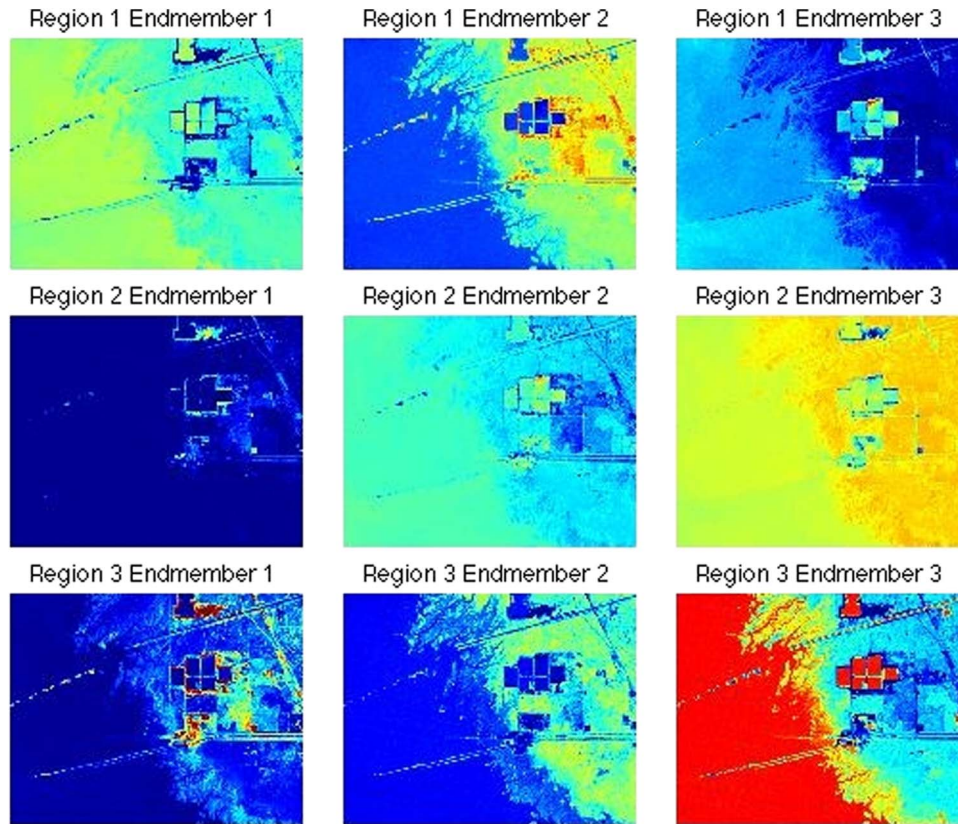
Fig. 11.   Abundance maps found on the 6-D Landsat TM data using PCOMMEND. The abundances shown are the values associated with the partition with the largest membership value for each data point. Each row corresponds to a convex region, and each image corresponds to the proportion map from one estimated endmember in the scene. The color scale ranges from (dark blue) zero to (red) one.

C. Landsat TM Data

PCOMMEND was also applied to 6-D Landsat TM data collected over the coast of Florida. The Landsat TM data considered contain 350×500 pixels. Analysis was conducted using the encoded radiance of these data. Within the image, there are suburban regions, vegetation, gulf water, and several large water reservoirs. A false-color image of the scene is shown in Fig. 10. The algorithm was applied to find three sets of three endmembers (for a total of nine endmembers). The resulting abundance maps are shown in Fig. 11. The Landsat TM collects data at the following six wavelength ranges for each band, respectively: 0.45–0.52, 0.52–0.60, 0.63–0.69, 0.76–0.90, 1.55–1.75, and 2.08–2.35 μm. Given that the Landsat TM data have only six dimensions, many endmember detection algorithms (such as ICE and VCA) are limited to finding at most seven endmembers for this data set. However, since PCOMMEND uses fuzzy clustering methods to partition the data set and can find a small number of endmembers for each partition, the restriction in the number of endmembers found can be avoided. Each row in Fig. 11 corresponds to one convex region. The first region can be interpreted as representing water from the gulf, water in reservoirs, and some roads. The second convex region corresponds mostly to what appears to be white sand in the imagery. The third region corresponds to vegetation in the scene.

This application illustrates another advantage of this piecewise convex endmember detection method which relates to determining endmembers for a large data set with a limited number of bands. Several existing endmember detection methods are restricted to finding $D + 1$ endmembers, where D is the number of bands in an image. Therefore, multispectral imagery is restricted, with these endmember detection methods, in the number of endmembers that can be extracted regardless of the number of true materials in the scene. Each individual convex piece can be up to $D + 1$ endmembers; however, the union of all of the endmembers for the scene can be greater than $D + 1$. One method that is used to circumvent this problem is to partition the imagery and find endmembers for each partition and then stitch the endmember results back together. However, it is difficult to determine how to partition the imagery and how to recombine endmember results. The proposed method autonomously groups the input data set and finds a set of endmembers for each group. The proposed PCOMMEND method removes the need to partition these data sets by hand and removes the need to manually combine the endmember results from each partition.

IV. DISCUSSION AND FUTURE WORK

PCOMMEND provides an endmember detection and spectral unmixing method that utilizes a piecewise convex representation of hyperspectral imagery. The piecewise convex representation allows several sets of endmembers to be determined. For each set of endmembers, the convex geometry model is applied, and spectral unmixing is performed. As the results indicate, the piecewise convex representation of hyperspectral

imagery provides a better representation of the input data sets when compared to a single convex region.

PCOMMEND consists of alternating optimization where the algorithm alternates between updating endmembers and updating abundance values. Both the endmembers and abundance values have a closed-form update, resulting in a much faster algorithm when compared to the sampling method used in [27]. In contrast, PCOMMEND applies a fuzzy clustering approach to the piecewise convex representation. Although the sampling approach is more likely to find a global optimum, PCOMMEND has the advantage over the Dirichlet process approach in that it is significantly faster. The previously published Dirichlet process approaches consider each pixel sequentially (using a Polya urn sampling scheme) which can result in this approach taking several hours to process a large image, whereas PCOMMEND can process all of the pixels in a batch mode taking several seconds. Additionally, a support-vector-machine-based endmember extraction (SVM-BEE) algorithm has been developed to extract endmembers from multiple distinct clusters in hyperspectral imagery [20]. The SVM-BEE approach identifies points in the imagery that lie on the edge of the convex hull of the clusters of the hyperspectral data, estimates the number of clusters in the data using the connectivity between the extracted support vectors, and then, for each cluster, performs dimensionality reduction and identifies the endmembers. However, in the SVM-BEE approach, the endmembers are restricted to points from the input data set, and this approach is unable to separate overlapping clusters of hyperspectral data. PCOMMEND, in contrast, can handle overlapping convex regions by assigning each data point a membership in each of the multiple convex regions. The fuzzy partition matrix estimated using PCOMMEND can be used to identify pixels that are found at the intersection of multiple endmember sets and may be composed of endmembers from many endmember sets. Both the Dirichlet process approach and the SVM-BEE approach create a crisp partition and cannot identify points in overlapping convex regions.

Future work for this method includes autonomously estimating the number of endmembers and the number of convex regions. Currently, we assume that the number of convex regions and the number of endmembers per cluster are known *a priori*. We are investigating relaxing this constraint by using an automatic estimation of these two parameters. Moreover, we plan to investigate an automatic determination of the number of endmembers per model and the balancing parameter α. We will extend the automatic determination of M that has been made in [37] to PCOMMEND.

As seen in the HySens Pavia University results, some materials were best unmixed using the piecewise convex representation in PCOMMEND. This warrants further investigation into the piecewise convex model for hyperspectral unmixing. However, in other materials, particularly materials found with several pure pixels in the scene, VCA outperformed the other methods due to its reliance on the pixel purity assumption. Future work for combining the advantages of these two approaches (methods that rely on the pixel purity assumption and methods that assumed highly mixed data sets) will be investigated.

REFERENCES

[1] N. Keshava and J. F. Mustard, "Spectral unmixing," *IEEE Signal Process. Mag.*, vol. 19, no. 1, pp. 44–57, Jan. 2002.

[2] B. Somers, G. P. Asner, L. Tits, and P. Coppin, "Endmember variability in spectral mixture analysis: A review," *Remote Sens. Environ.*, vol. 115, no. 7, pp. 1603–1616, Jul. 2011.

[3] J. M. Bioucas-Dias, A. Plaza, N. Dobigeon, M. Parente, Q. Du, and P. Gader, "Hyperspectral unmixing overview: Geometrical, statistical, and sparse regression-based approaches," *IEEE J. Sel. Topics Appl. Earth Observ. Remote Sens.*, vol. 5, no. 2, pp. 354–379, Apr. 2012.

[4] M. E. Winter, "Fast autonomous spectral end-member determination in hyperspectral data," in *Proc. 13th Int. Conf. Appl. Geol. Remote Sens.*, Vancouver, BC, Canada, 1999, pp. 337–344.

[5] J. Boardman, F. Kruse, and R. Green, "Mapping target signatures via partial unmixing of AVIRIS data," in *Summaries of the 5th Annu. JPL Airborne Geoscience Workshop*, vol. 1, R. Green, Ed. Pasadena, CA: JPL Publ., 1995, pp. 23–26.

[6] J. M. P. Nascimento and J. M. Bioucas-Dias, "Vertex component analysis: A fast algorithm to unmix hyperspectral data," *IEEE Trans. Geosci. Remote Sens.*, vol. 43, no. 4, pp. 898–910, Apr. 2005.

[7] A. Plaza, P. Martinez, R. Perez, and J. Plaza, "Spatial/spectral endmember extraction by multidimensional morphological operators," *IEEE Trans. Geosci. Remote Sens.*, vol. 40, no. 9, pp. 2025–2041, Sep. 2002.

[8] C.-I. Chang, C.-C. Wu, C.-S. Lo, and M.-L. Chang, "Real-time simplex growing algorithms for hyperspectral endmember extraction," *IEEE Trans. Geosci. Remote Sens.*, vol. 48, no. 4, pp. 1834–1850, Apr. 2010.

[9] D. Thompson, L. Mandrake, M. Gilmore, and R. Castano, "Superpixel endmember detection," *IEEE Trans. Geosci. Remote Sens.*, vol. 48, no. 11, pp. 4023–4033, Nov. 2010.

[10] T.-H. Chan, W. K. Ma, A. Ambikapathi, and C.-Y. Chi, "A simplex volume maximization framework for hyperspectral endmember extraction," *IEEE Trans. Geosci. Remote Sens.*, vol. 49, no. 11, pp. 4177–4193, Nov. 2011.

[11] D. Lee and H. Seung, "Algorithms for non-negative matrix factorization," *Adv. Neural Inf. Process. Syst.*, vol. 13, pp. 556–562, 2000.

[12] L. Miao and H. Qi, "Endmember extraction from highly mixed data using minimum volume constrained nonnegative matrix factorization," *IEEE Trans. Geosci. Remote Sens.*, vol. 45, no. 3, pp. 765–777, Mar. 2007.

[13] V. P. Pauca, J. Piper, and R. J. Plemmons, "Nonnegative matrix factorization for spectral data analysis," *Linear Algebra Appl.*, vol. 416, no. 1, pp. 321–331, Jul. 2005.

[14] S. Jia and Y. Qian, "Constrained nonnegative matrix factorization for hyperspectral unmixing," *IEEE Trans. Geosci. Remote Sens.*, vol. 47, no. 1, pp. 161–173, Jan. 2009.

[15] T.-M. Tu, "Unsupervised signature extraction and separation in hyperspectral images: A noise-adjusted fast independent components analysis approach," *Opt. Eng.*, vol. 39, no. 4, pp. 897–906, Apr. 2000.

[16] J. Wang and C.-I. Chang, "Applications of independent component analysis in endmember extraction and abundance quantification for hyperspectral imagery," *IEEE Trans. Geosci. Remote Sens.*, vol. 44, no. 9, pp. 2601–2616, Sep. 2006.

[17] M. D. Craig, "Minimum-volume transforms for remotely sensed data," *IEEE Trans. Geosci. Remote Sens.*, vol. 32, no. 3, pp. 542–552, May 1994.

[18] G. X. Ritter, G. Urcid, and M. S. Schmalz, "Autonomous single-pass endmember approximation using lattice auto-associative memories," *Neurocomputing*, vol. 72, no. 10–12, pp. 2101–2110, Jun. 2009.

[19] M. Berman, H. Kiiveri, R. Lagerstrom, A. Ernst, R. Dunne, and J. F. Huntington, "ICE: A statistical approach to identifying endmembers in hyperspectral images," *IEEE Trans. Geosci. Remote Sens.*, vol. 42, no. 10, pp. 2085–2095, Oct. 2004.

[20] A. Filippi and R. Archibald, "Support vector machine-based endmember extraction," *IEEE Trans. Geosci. Remote Sens.*, vol. 47, no. 3, pp. 771–791, Mar. 2009.

[21] M. Iordache, J. Bioucas-Dias, and A. Plaza, "Sparse unmixing of hyperspectral data," *IEEE Trans. Geosci. Remote Sens.*, vol. 49, no. 6, pp. 2014–2039, Jun. 2011.

[22] G. P. Asner and D. B. Lobell, "A biogeophysical approach for automated SWIR unmixing of soils and vegetation," *Remote Sens. Environ.*, vol. 74, no. 1, pp. 99–112, Oct. 2000.

[23] C. A. Bateson, G. P. Asner, and C. A. Wessman, "Endmember bundles: A new approach to incorporating endmember variability into spectral mixture analysis," *IEEE Trans. Geosci. Remote Sens.*, vol. 38, no. 2, pp. 1083–1093, Mar. 2000.

[24] P. E. Dennison and D. A. Roberts, "Multiple endmember spectral mixture analysis using endmember average RSME," *Remote Sens. Environ.*, vol. 87, no. 2/3, pp. 123–135, Oct. 2003.

[25] D. A. Roberts, M. Gardner, R. Church, S. Ustin, G. Scheer, and R. O. Green, "Mapping chaparral in the Santa Monica Mountains using multiple endmember spectral mixture models," *Remote Sens. Environ.*, vol. 65, no. 3, pp. 267–279, Sep. 1998.

[26] A. Zare, J. Bolton, P. Gader, and M. Schatten, "Vegetation mapping for landmine detection using long wave hyperspectral imagery," *IEEE Trans. Geosci. Remote Sens.*, vol. 46, no. 1, pp. 172–178, Jan. 2008.

[27] A. Zare and P. Gader, "PCE: Piece-wise convex endmember detection," *IEEE Trans. Geosci. Remote Sens.*, vol. 48, no. 6, pp. 2620–2632, Jun. 2010.

[28] A. Zare and P. Gader, "Context-based endmember detection for hyperspectral imagery," in *Proc. 1st IEEE Workshop Hyperspectral Image Signal Process., Evol. Remote Sens.*, Grenoble, France, Aug. 2009, pp. 1–4.

[29] O. Eches, N. Dobigeon, C. Mailhes, and J. Tourneret, "Bayesian estimation of linear mixtures using the normal compositional model," *IEEE Trans. Image Process.*, vol. 19, no. 11, pp. 1403–1413, Jun. 2010.

[30] A. Zare, "Hyperspectral endmember detection and band selection using Bayesian methods," Ph.D. dissertation, Univ. Florida, Gainesville, FL, 2009.

[31] H. W. Kuhn and A. W. Tucker, "Nonlinear programming," in *Proc. 2nd Berkeley Symp.*, 1951, pp. 481–492.

[32] D. T. Anderson and A. Zare, "Spectral unmixing cluster validity index for multiple sets of endmembers," *IEEE J. Sel. Topics Appl. Earth Observ. Remote Sens.*, vol. 5, no. 4, pp. 1281–1295, Aug. 2012.

[33] A. M. Baldridge, S. J. Hook, C. I. Grove, and G. Rivera, "The ASTER spectral library version 2.0," *Remote Sens. Environ.*, vol. 113, no. 4, pp. 711–715, Apr. 2009.

[34] F. A. Kruse, A. B. Lefkoff, J. B. Boardman, K. B. Heidebrecht, A. T. Shapiro, P. J. Barloon, and A. F. H. Goetz, "The spectral image processing system (SIPS)—Interactive visualization and analysis of imaging spectrometer data," *Remote Sens. Environ.*, vol. 44, no. 2/3, pp. 145–163, May/Jun. 1993.

[35] C.-I. Chang, "An information-theoretic based approach to spectral variability, similarity, and discriminability for hyperspectral image analysis," *IEEE Trans. Inf. Theory*, vol. 46, no. 5, pp. 1927–1932, Aug. 2000.

[36] S. Holzwarth, A. Muller, M. Habermeyer, R. Richter, A. Hausold, S. Thiemann, and P. Strobl, "Hysens—Dais 7915/ ROSIS imaging spectrometers at DLR," in *Proc. 3rd EARSeL Workshop Imaging Spectrosc.*, May 2003, pp. 3–14.

[37] A. Zare and P. Gader, "Sparsity promoting iterated constrained endmember detection for hyperspectral imagery," *IEEE Geosci. Remote Sens. Lett.*, vol. 4, no. 3, pp. 446–450, Jul. 2007.

Alina Zare (S'07–M'08) received the Ph.D. degree from the University of Florida, Gainesville, in 2008.

She is currently an Assistant Professor with the Department of Electrical and Computer Engineering, University of Missouri, Columbia. Her research interests include machine learning, Bayesian methods, sparsity promotion, image analysis, pattern recognition, hyperspectral image analysis, and human geography.

Paul Gader (M'86–SM'09–F'11) received the Ph.D. degree in mathematics for image-processing-related research from the University of Florida, Gainesville, in 1986.

He was a Senior Research Scientist with Honeywell, a Research Engineer and a Manager with the Environmental Research Institute of Michigan, and a Faculty Member with the University of Wisconsin, Oshkosh, the University of Missouri, Columbia, and the University of Florida, where he is currently a Professor and the Interim Chair of Computer and Information Science and Engineering. He performed his first research in image processing in 1984 working on algorithms for detection of bridges in forward-looking infrared imagery as a Summer Student Fellow at Eglin Air Force Base. His dissertation research focused on algebraic methods for parallel image processing. He has since worked on a wide variety of theoretical and applied research problems including fast computing with linear algebra, mathematical morphology, fuzzy sets, Bayesian methods, handwriting recognition, automatic target recognition, biomedical image analysis, landmine detection, human geography, and hyperspectral and Light Detection and Ranging image analysis projects. He has published hundreds of refereed journal and conference papers.

Prof. Gader became a Fellow of the IEEE for his work in land-mine detection.

Ouiem Bchir received the Ph.D. degree from the University of Louisville, Louisville, KY.

She is currently an Assistant Professor with the Computer Science Department, College of Computer and Information Sciences, King Saud University, Riyadh, Saudi Arabia. Her research interests are spectral and kernel clustering, pattern recognition, hyperspectral image analysis, local distance measure learning, and unsupervised and semisupervised machine learning techniques.

Dr. Bchir was the recipient of the University of Louisville Dean's Citation, the University of Louisville Computer Science and Engineering Doctoral Award, and the Tunisian Presidential Award for the electrical engineering diploma.

Hichem Frigui (S'92–M'98) received the Ph.D. degree in computer engineering and computer science from the University of Missouri, Columbia, in 1997.

From 1998 to 2004, he was an Assistant Professor with The University of Memphis, Memphis, TN. He is currently a Professor with the University of Louisville, Louisville, KY, where he is also the Director of the Multimedia Research Laboratory. He has been active in the research fields of fuzzy pattern recognition, data mining, and image processing with applications to content-based multimedia retrieval and land-mine detection. He has participated in the development, testing, and real-time implementation of several land-mine detection systems. He has published over 135 journal and refereed conference articles.

Dr. Frigui was a recipient of the National Science Foundation Career Award for outstanding young scientists.